Oxidation of Metals, Vol. 31, Nos. 3/4, 1989

Effect of the θ–α-Al_2O_3 Transformation on the Oxidation Behavior of β-NiAl + Zr

George C. Rybicki* and James L. Smialek*†

Received June 23, 1988

Isothermal oxidation of NiAl + Zr has been performed over the temperature range of 800–1200°C and studied by TGA, XRD, and SEM. A discontinuous decrease in growth rate of two orders of magnitude was observed at 1000°C due to the formation of α-Al_2O_3 from θ-Al_2O_3. This transformation also resulted in a dramatic change in the surface morphology of the scales, as a whisker topography was changed into a weblike network of oxide ridges and radial transformation cracks. It is believed that the ridges are evidence for a short-circuit outward aluminum diffusion growth mechanism that has been documented in a number of ^{18}O tracer studies.

KEY WORDS: NiAl; Al_2O_3 scales; oxide ridges.

INTRODUCTION

β-NiAl remains as a material of interest in high-temperature aerospace applications because of its excellent oxidation resistance. Although its primary role in the past has been as an oxidation resistant coating for superalloys, it is currently being considered as a matrix material for advanced fiber-reinforced composites.[1] In this application, its high melting point (1640°C) and good oxidation resistance overshadow its relatively poor high-temperature strength.

The oxidation resistance of β-NiAl is attributable to the exclusive formation of α-Al_2O_3 scales and their corresponding low growth kinetics.[2] Cyclic oxidation studies performed at 1100° and 1200°C have shown that some degradation may occur because of spalling, especially if it occurs at

*NASA Lewis Research Center, Cleveland, Ohio 44135.
†To whom correspondence should be addressed.

0030-770X/89/0400-0275$06.00/0

the oxide-metal interface.[3-5] However, recent studies show that Zr-doping to about 0.1 wt.% is sufficient to prevent spalling to bare metal and results in excellent behavior at 1200°C for up to 3000 1-hr cycles.[6,7] Improvements in both kinetics and adhesion have also been achieved by ion implantation of 10^{16} Y atoms/cm^2 into NiAl.[8] Substantial grain growth may occur in the scales at 1200° and 1300°C, which significantly reduces oxidation kinetics; therefore grain boundary diffusion is considered to be a major contribution to the overall scale growth process.[9]

In an effort to produce adherent, highly oriented scales, single crystals of Zr-doped β-NiAl were oxidized and studied by transmission electron microscopy (TEM) techniques.[10-15] At low temperatures (800°C), highly epitaxial single-crystal transition alumina scales were produced on (001), (011), (111), and (012) NiAl planes. Most of these scale structures were based on the cubic γ-phase; however, θ-Al_2O_3 was the predominant phase after 1 hr at 800°C, persisting up to $\geq$100 hr. The crystallographic relationships between oxide and metal commonly maintained a close match up between the interplanar spacings of the aluminum sublattice in the oxide and those in the metal. However, this single crystal structure was not retained upon heating to 1100°C, as individual nuclei of rhombohedral α-Al_2O_3 formed between 1 to 10 hr and grew into large plates of textured subgrains.

The purpose of the present study is to document the dramatic morphological and kinetic changes that accompany this transformation. Particular attention is paid to the origin of the distinctive oxide ridge structure previously reported for alumina scales formed on NiAl, FeCrAl, and Pt-Al alloys.[5,9,11,16-19]

EXPERIMENTAL PROCEDURE

Directionally solidified bars of NiAl + Zr were obtained with the overall dimensions of 1.3 × 2.5 × 15 cm.* Chemical analysis revealed that in addition to the intentionally added 29.35 wt.% Al and 0.11 wt.% Zr, (47.2 at.% Al and 0.05 at.% Zr), the following impurities were also present: 0.2 wt.% Si, 0.1 wt.% Fe, 0.042 wt.% Cr, 0.004 wt.% Ti, and 0.002 wt.% Y. Test coupons 0.3 × 1.3 × 2.5 cm were electrodischarge machined from the bars, polished through 600-grit SiC, and ultrasonically cleaned in detergent, then in ethanol.

The coupons were oxidized in a platinum wound furnace using a 1.9-cm inner-diameter (ID) alumina tube and dry air flowing at 280 cc/min. Oxidation temperatures were 800, 900, 1000, 1100, and 1200°C. Weight change was monitored continually by means of an electrobalance† and data were

*TRW, Inc.
†Cahn 1000.

collected by a microcomputer‡ every 30 sec for the first 10 min and every 6 min thereafter.

The weight gains were corrected for buoyancy effects and platinum hanger wire evaporation losses. Buoyancy was determined from calibration runs with inert MgO coupons of the same dimensions as the oxidation coupons. Linear weight loss rates of the platinum wires were measured over the 800–1200°C experimentation range. Oxide scale phases were identified from X-ray diffractometer (XRD) scans, and surface morphology was examined by scanning electron microscopy (SEM).

RESULTS

Kinetics

The weight-gain curves (linear plots) for all five temperatures are shown in Fig. 1. The important point is that the final weight gains at 100 hr are successively higher for higher temperatures except for the 900°C test. Exposure at this temperature produced weight gains actually higher than for the 1000 or 1100°C tests. This fact illustrates the key point of this paper, i.e., that a phase transition occurs in Al_2O_3 scales at intermediate temperatures; this results in a major decrease in kinetics.

At the extremes of temperature, 800° or 1200°C, essentially parabolic kinetics were observed as shown in the plots of (weight gain)^2 versus time

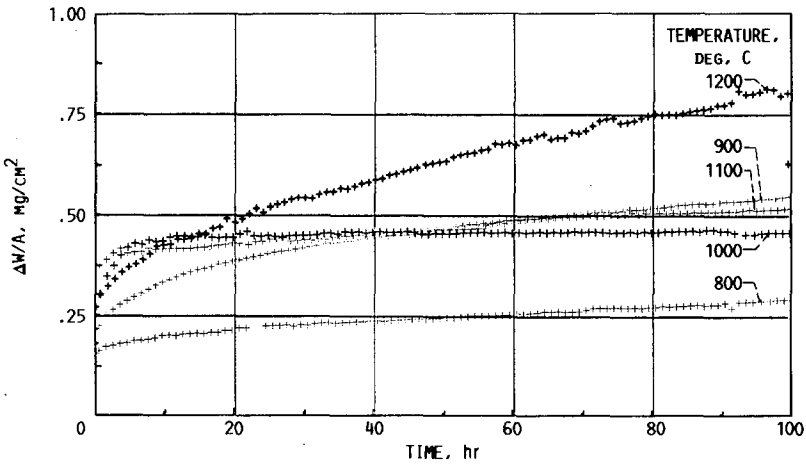

Fig. 1. Effect of temperature on isothermal oxidation weight gain curves for NiAl + 0.1 Zr.

‡Hewlett Packard HP-85.

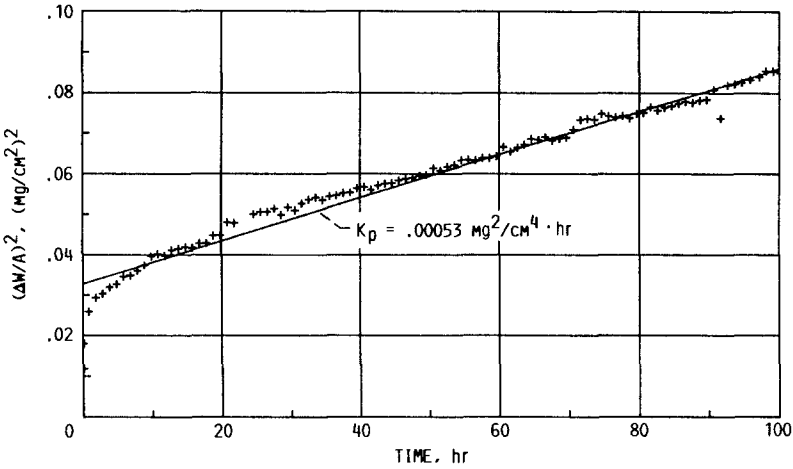

Fig. 2. Parabolic square plot for NiAl+Zr isothermal oxidation at 800°C.

in Figs. 2 and 3. (This method is justified in a later section.) Least-squares analysis was used to fit straight lines to the data and derive values of k_p. At 1000°C, a distinct break in the square plot occurs at about 8 hr (Fig. 4). After this break, the parabolic rate constant was lower by two orders of magnitude. This type of behavior was reproduced by a duplicate run at 1000°C, indicating that the effect was real and not spurious.

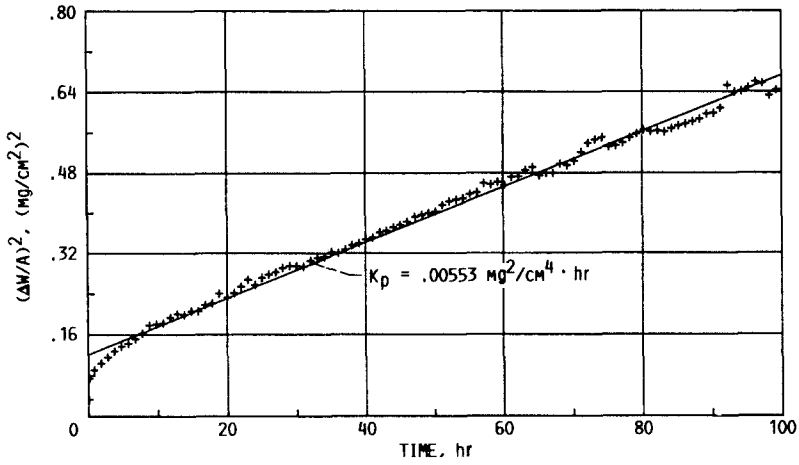

Fig. 3. Parabolic square plot for NiAl+Zr isothermal oxidation at 1200°C.

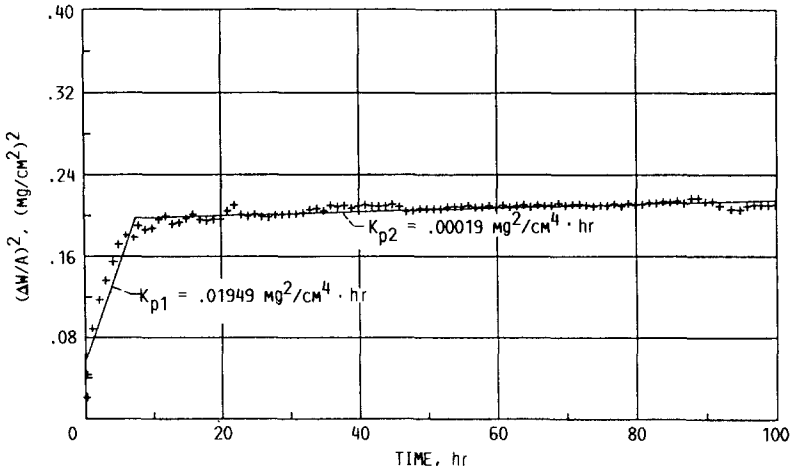

Fig. 4. Bimodal isothermal oxidation kinetics for NiAl+Zr at 1000°C.

The temperature dependence of k_p can be seen in the Arrhenius plot of Fig. 5. Here, two completely distinct branches correspond to low- and high-temperature behavior. At 1000°C, the initial k_{p1} (<8 hr) falls on the low-temperature branch, while the secondary k_{p2} fits the high-temperature line. Below 1000°C, the scale remains as θ-Al_2O_3 for the 100-hr test, while

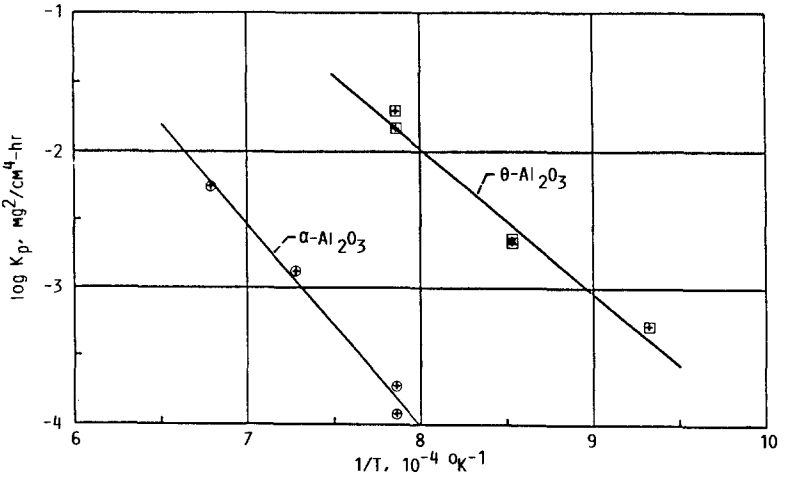

Fig. 5. Arrhenius plot of k_p for transition θ-Al_2O_3 scales and mature α-Al_2O_3 scales formed on NiAl+Zr.

above 1000°C the transformation occurs quite early so as not to contribute significantly to the kinetics. Thus, the low- and high-temperature Arrhenius behavior can be described by two least-square fits to the data:

$$k_{p\theta}\ (\text{low}) = 1.24 \times 10^7 \exp(-51.4\ \text{kcal}/RT)\ \text{mg}^2/\text{cm}^4 \cdot \text{hr}$$

$$k_{p\alpha}\ (\text{high}) = 6.77 \times 10^7 \exp(-67.4\ \text{kcal}/RT)\ \text{mg}^2/\text{cm}^4 \cdot \text{hr}$$

X-Ray Diffraction

The oxide diffraction peaks are listed in Table I. The best identification of the low-temperature scale is δ or θ-Al_2O_3, even though many peaks were absent and the relative intensities departed from the published values. Preferred orientation could account for these differences in intensity. Also, the 2.43-Å peak changed from the strongest to the weakest for the 800° and 900°C samples, suggesting different preferred orientations for different samples. Doychak identified δ-Al_2O_3 (after 0.1 hr) and θ-Al_2O_3 (after 1–100 hr) by electron diffraction in his TEM studies of the same NiAl+Zr material oxidized at 800°C.[10–15] Doychak and associates have also shown very strong orientation relationships between the scales and various single crystal NiAl sample faces. It should also be noted that the precise crystal structure of δ-Al_2O_3 has not been formulated, and discrepancies in the JCPDS card 16-394 for δ still exist. In fact, in a recent TEM study of the oxide crystal structures formed on Udimet 700, it is proposed that θ-Al_2O_3 is the correct identification of these low temperature scales and even that no δ-phase ever exists distinct from θ.[20]

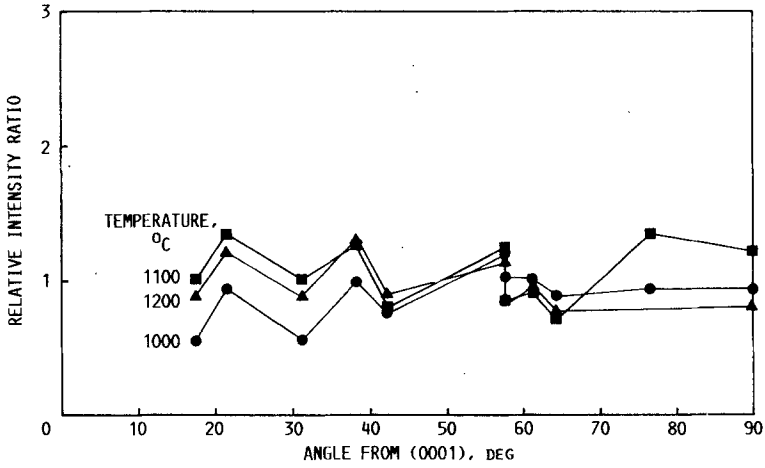

Fig. 6. Inverse pole figure for α-Al_2O_3 scales formed on NiAl+Zr after 100-hr isothermal oxidation.

By contrast, the identification of α-Al_2O_3 in Table I was much more straightforward. The higher-temperature scales contained all the major peaks in about the correct relative intensities. Inverse pole figures were constructed for the (0001) plane to determine whether any preferred α orientation persisted after the transition from θ (Fig. 6). The relative intensity of any diffraction peak is scaled to the same peak of a perfectly random α-Al_2O_3 powder sample and plotted against the (*hkil*)-(0001) interplanar angle. No systematic deviation from unity, i.e., no preferred orientation, was discerned for these α-Al_2O_3 scales.

The trend toward α-Al_2O_3 with longer times and higher temperatures, as suggested in Table I, is shown graphically in Fig. 7. Here the total diffracted intensity is used as a qualitative indication of the amount of each phase present after 100 hr. Below ~1000°C θ-Al_2O_3 is seen to be the predominant scale phase and α-Al_2O_3 above 1000°C. Only a trace of α was present at 900°C. Although no θ-Al_2O_3 was observed at 1000°C after 100 hr (solid data points), a substantial amount existed at 5 hr (open data points). This finding is consistent with the parabolic plot of Fig. 4, which shows a distinct change in kinetics at ~8 hr. The transformation from θ to α-Al_2O_3 scales was responsible for this change. The persistence of θ out to 100 hr at 800 and 900°C and the transition to kinetic control solely by α at 1100 and 1200°C accounts for the two branches in the Arrhenius plot. Thus, both transformations with oxidation time and transitions with oxidation temperature need to be accounted for in describing NiAl scale growth kinetics and morphologies.

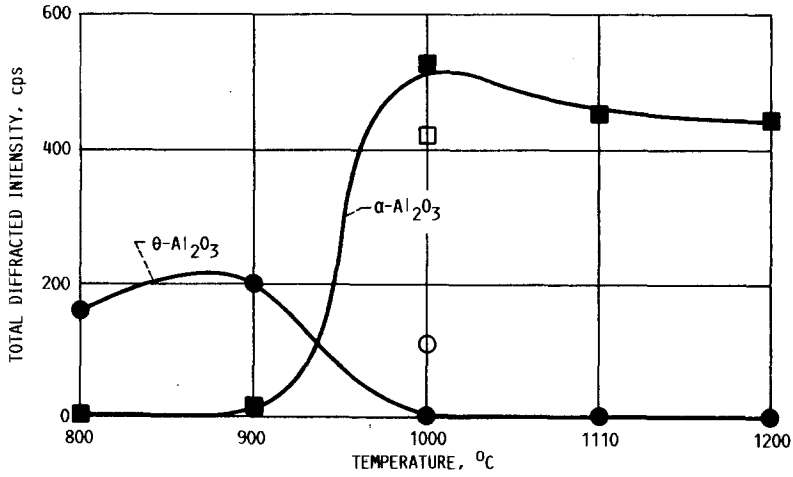

Fig. 7. Transition in scale phases, as determined by X-ray diffraction, formed on NiAl+Zr after 100-hr isothermal oxidation. Open symbols refer to 5-hr oxidation.

Table I. X-Ray Diffraction Peaks and Phase Identification of Oxide Scales on NiAl+Zr: d spacings (Å) and I/I_{100} relative intensities

Published (major)						Experimental											
δ-Al_2O_3 (16-394)			θ-Al_2O_3 (23-1009)			800°C/100 hr		900°C/100 hr		1000°C/5 hr		1000°C/100 hr		1100°C/100 hr		1200°C/100 hr	
hkl	d(Å)	I/I_{100}	*hkl*	d(Å)	I/I_{100}	d(Å)	I/I_{100}	d(Å)	I/I_{100}	d(Å)	I/I_{100}	d(Å)	I/I_{100}	d(Å)	I/I_{100}	d(Å)	I/I_{100}
			001	5.45	10												
113	4.57	12	$20\bar{1}$	4.54	18			4.55	5								
114,105	4.07	12															
117	2.88	8	$400, 40\bar{1}$	2.84	80			2.87	12								
222	2.73	30	202, 002	2.73	65	2.74	50	2.74	100	2.74	60						
302, 118	2.60	25	$11\bar{1}$	2.57	14												
312	2.46	60	111	2.44	60	2.43	100	2.43	6								
313	2.40	16	401, 310	2.32	45												
226	2.28	40	$40\bar{2}$, 202	2.26	35												
400	1.99	75	$31\bar{1}$, $11\bar{2}$	2.02	45	2.02	100	2.02	7								
0·0·12	1.95	40	$60\bar{1}$	1.95	8												
318	1.91	12	600, $31\bar{2}$	1.91	30			1.91	6								
319	1.81	8	510	1.80	14												
513	1.54	8	313	1.54	25												
1·1·15	1.52	16	113, $80\bar{1}$	1.49	25												
523, 516	1.46	8	020	1.45	25												
440	1.41	50															
4·0·12	1.40	100	$71\bar{2}$, 512	1.39	100	1.40	60	1.40	60	1.40	60						

α-Al_2O_3 (10–173)												
hkl	*d*(Å)	I/I_{100}										
$01\bar{1}2$	3.48	75				3.48	65	3.48	65	3.48	60	3.48	50
$10\bar{1}4$	2.55	90				2.55	75	2.55	90	2.55	100	2.55	100
$11\bar{2}0$	2.38	40				2.38	40	2.38	60	2.38	40	2.38	25
$11\bar{2}3$	2.09	100	2.08	8		2.09	100	2.09	100	2.09	80	2.09	80
$02\bar{2}4$	1.74	45	1.74	5		1.74	45	1.74	45	1.75	30	1.75	30
$11\bar{2}6$	1.60	80				1.60	65	1.60	65	1.60	60	1.60	65
$21\bar{3}1$	1.55	4						1.55	7	1.55	5	1.55	5
$12\bar{3}2,11\bar{2}8$	1.51	14						1.51	7	1.51	9	1.51	8
$12\bar{3}4$	1.40	30				1.40	50	1.40	30	1.40	20	1.41	20
$03\bar{3}0$	1.37	50				1.37	35	1.37	45	1.38	30	1.37	30

The large amount of α present after 5 hr at 1000°C (Fig. 7), when the kinetics appear to be controlled by θ, cannot be easily explained. α is observed to be nucleated at the gas surface for both bulk and thermally grown transition alumina.[15,21] It may therefore show a disproportionately large effect on the amount of diffracted intensity.

Morphology

The surface morphology of the θ-Al_2O_3 scales formed at 800 and 900°C is shown in Fig. 8. The 800°C scale contained finely textured or nodular features aligned with polishing marks. The size of the individual nodules was on the order of 0.3 μm or less. At 900°C, whiskers were observed on the order of 0.5 μm wide $\times$ 5 μm long, probably representing outgrowths of the lower temperature nodules. The relative intensity of the $(20\bar{2})_\theta$ peak is also two times stronger than expected, implying a preferred growth direction of the needles.

The nucleation of α-Al_2O_3 from a matrix of θ-Al_2O_3 can be seen in the transition structure obtained after 5 hr at 1000°C (Fig. 9). Basically, the θ structure is a combination of nodules and whiskers as seen at the lower temperatures. The α-phase appears as dark, flat, 10-μm circular regions containing radial cracks. This morphology was maintained after the transformation had been completed at 100 hr (Fig. 10). However, the frequency of the platelets has increased to the extent that they occupied nearly the entire surface.

The absence of any indication of θ-Al_2O_3 formation at the higher temperatures is reflected in the dramatically different microstructures obtained at 1100 and 1200°C (Fig. 11). Here nodules or whiskers were less apparent; instead, a network of oxide ridges or the lacy structure developed. The network often assumed a cellular appearance in which the cell diameters were 10–20 μm wide and radial spokes divided each cell into 1- to 5-μm wide segments. These dimensions are similar to the 10 μm α-Al_2O_3 platelets found at 1000°C; the radial spokes are reminiscent of the radial cracks in those platelets.

Optical microscopy was also useful in following the course of the transformation. The early stages at 1000°C after 5 hr can be distinctly observed in Fig. 12a. Here the scale is still primarily θ-Al_2O_3, with bright appearing cells of α-Al_2O_3. At 1100 and 1200°C, these reflective cells occupy the entire surface (Fig. 12b,c), and surface smoothing has eliminated most of the dark whisker regions.

DISCUSSION

A self-consistent picture of the above data is that at low temperatures NiAl forms fast-growing transition alumina via outward cation diffusion.

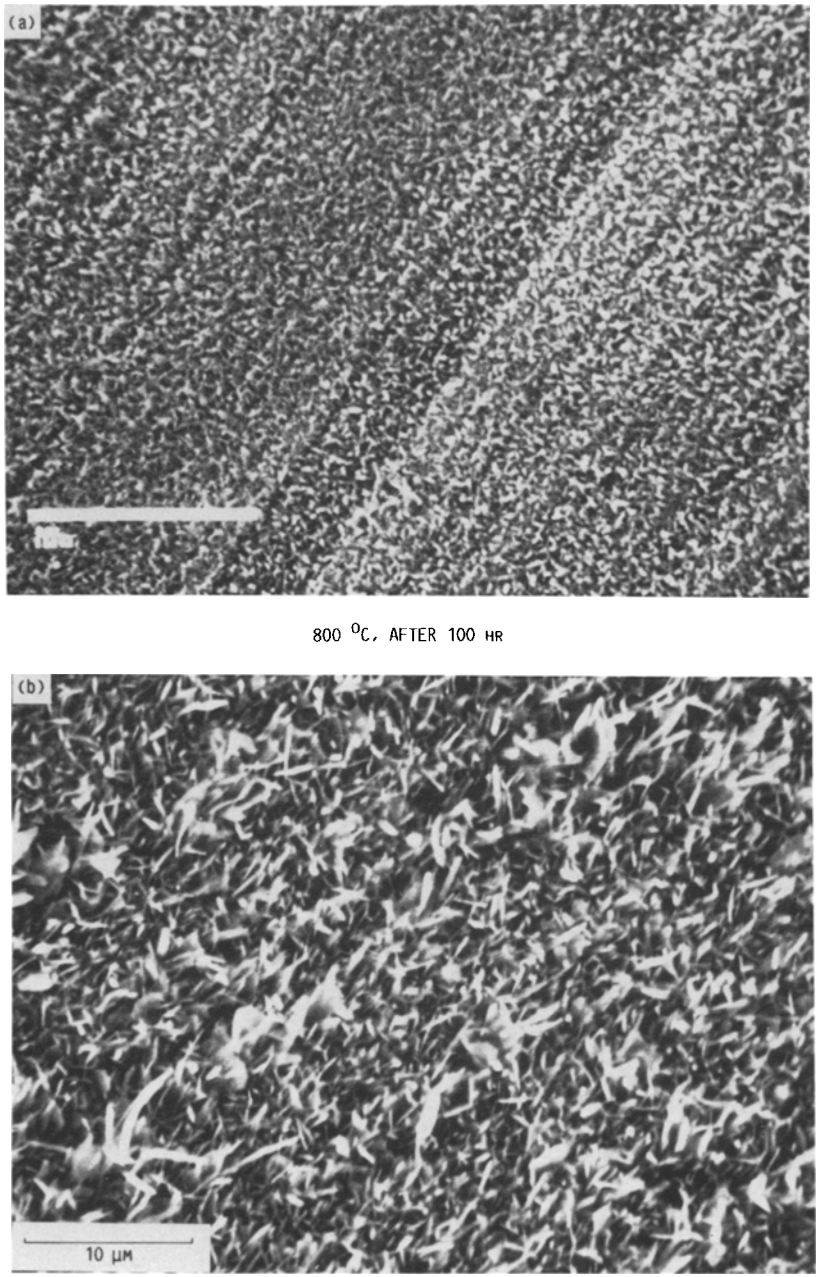

Fig. 8. Development of θ-Al_2O_3 whisker morphology on NiAl + Zr after 100-hr oxidation. (a) 800°C. (b) 900°C.

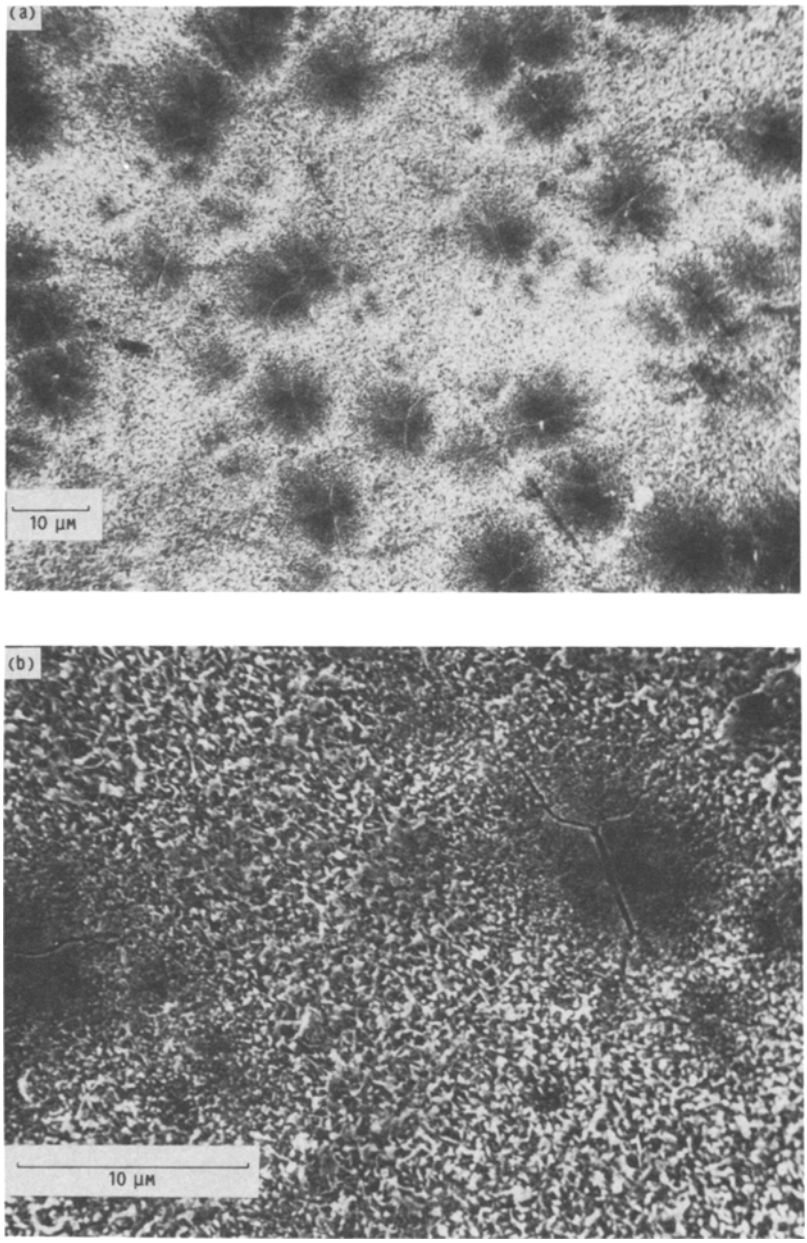

Fig. 9. Nucleation of circular platelets of α-Al_2O_3 in a matrix of θ-Al_2O_3 whiskers after 5-hr oxidation at 1000°C. (a) Overview. (b) Cracks in platelets.

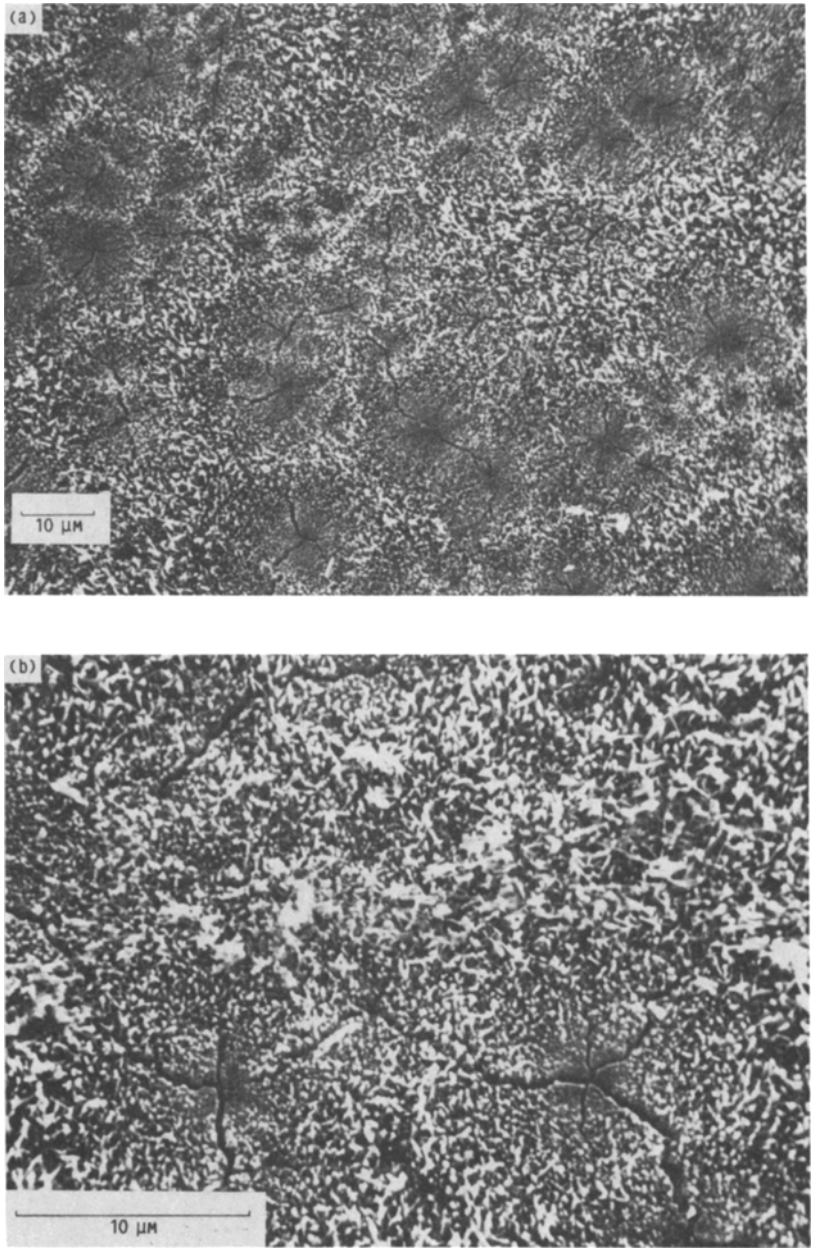

Fig. 10. Completed transformation to α-Al_2O_3 platelets after 100-hr oxidation at 1000°C. (a) Overview. (b) Cracks in platelets.

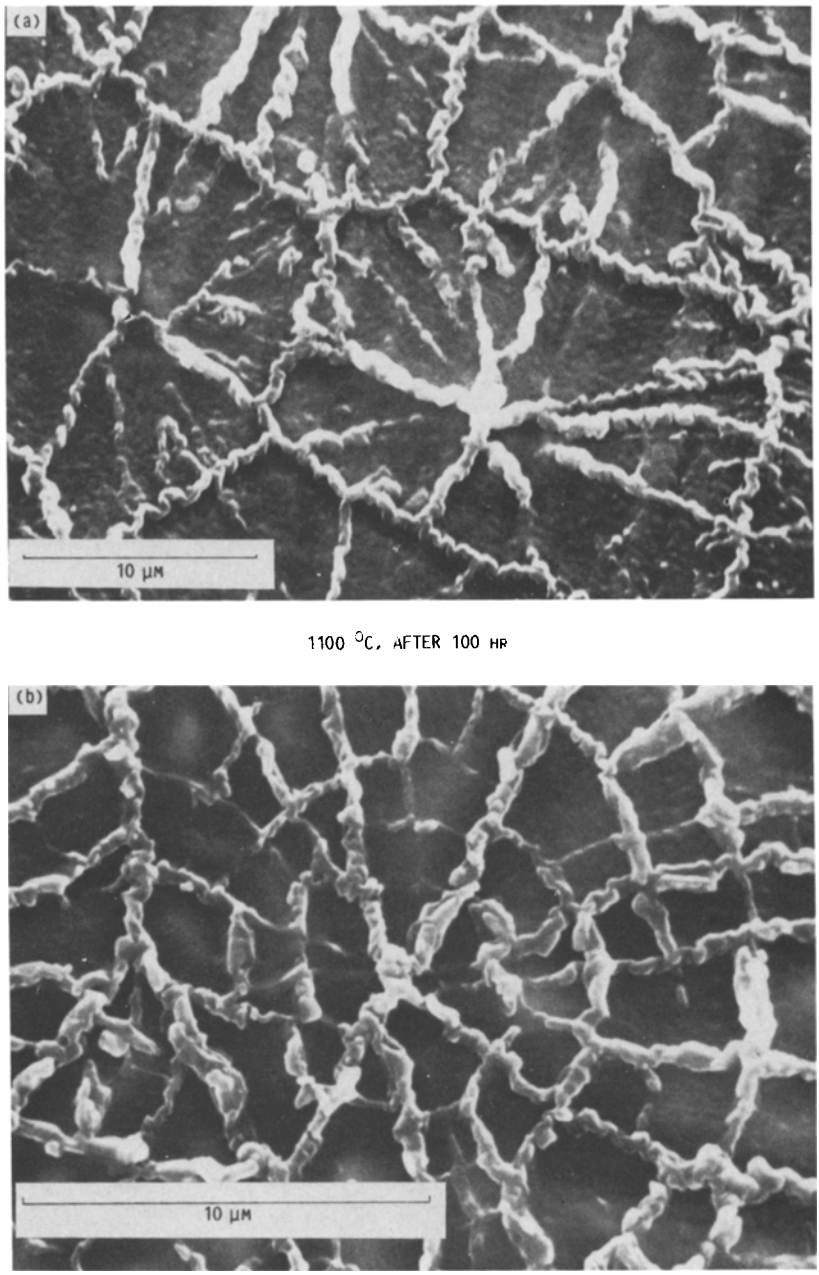

Fig. 11. Fully developed ridge structure in mature α-Al_2O_3 scales formed after 100-hr oxidation. (a) 1100°C. (b) 1200°C.

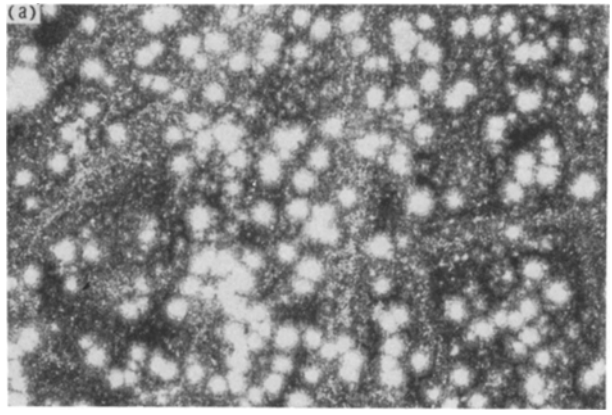

(a) 1000 °C, 5 HR.

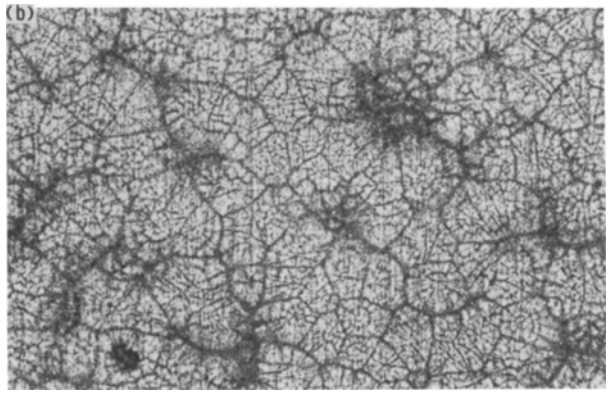

(b) 1100 °C, 100 HR.

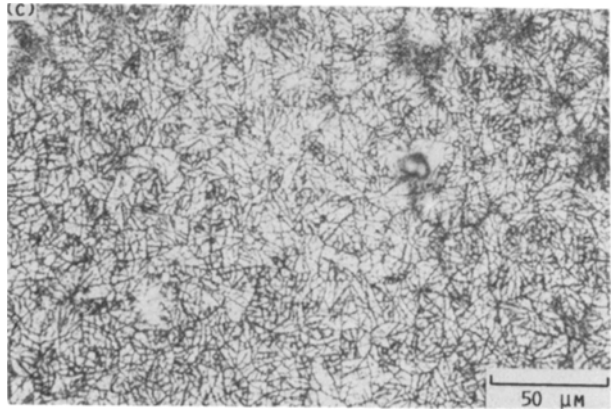

(c) 1200 °C, 100 HR.

Fig. 12. Optical micrographs highlighting the formation of circular α-Al_2O_3 platelets. (a) Initial nucleation after 5 hr at 1000°C. (b) Total transformation after 100 hr at 1100°C. (c) Total transformation after 100 hr at 1200°C.

At about 1000°C, these transition scales transform to α-Al_2O_3, resulting in substantial contraction stresses and cracking. Growth kinetics are substantially reduced because of lower diffusivities in the nearly close-packed corundum structure. The peculiar ridge network is a vestige of high-diffusivity paths left by impinging α-cells, radial cracks, and radial subgrain boundaries in the transformed α-Al_2O_3.[11,14,15] The resulting growth mechanism is a complex mix of inward and outward diffusion controlled by microstructure. The following discussion relates this picture to similar concepts previously put forward by other investigators.

Kinetics

The growth rates of transition aluminas have not been widely studied. Figure 13 summarizes the existing data presented by Hutchings and Loretto[22]

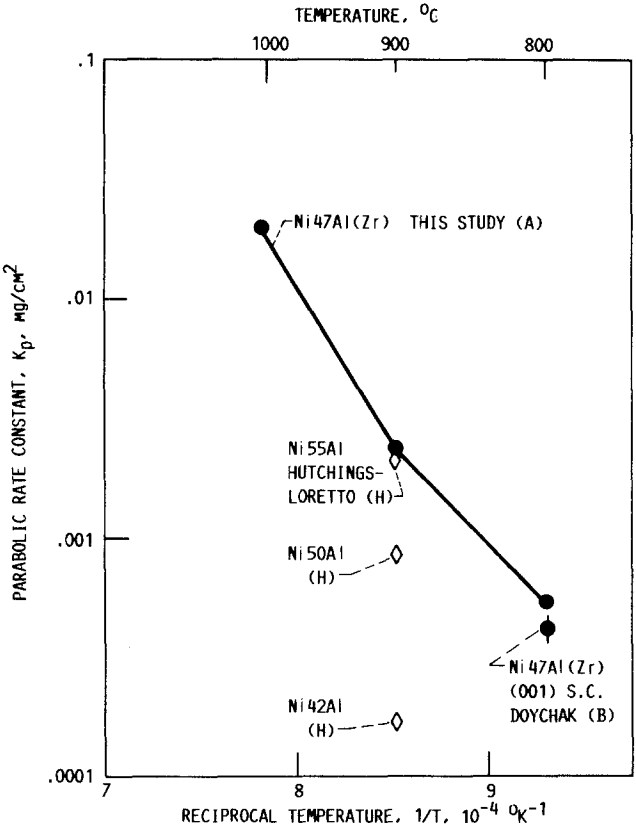

Fig. 13. Arrhenius plot of low-temperature k_p data compared with data of other NiAl studies. (See Table II for data code.)

at 900°C and of Doychak at 800°C.[11] A large increase in k_p was found with increasing aluminum content in the former study.[22] Oxidation of single crystals proceeded at about 20% lower rates than did polycrystals in both studies. These investigators also found significant rate decreases due to electropolishing as compared with 600- or 1200-grit sanding.

The growth rates for α-Al_2O_3 scales on β-NiAl (i.e., above 1000°C) have been more widely studied (Fig. 14; Table II). Some compositional differences existed between the β-NiAl alloys studied by various investigators. However, no consistent trend with aluminum content can be discerned because changes in test procedure usually occurred from study to study. The work of Jedlinski and Mrowec shows about a two-fold rate reduction due to ion implantation of 10^{16} Y atoms/cm^2. (These data were taken from their thickness vs $t^{1/2}$ curves, converted to weight change, assuming 5.339 μm for 1 mg/cm^2 for α-Al_2O_3.[8] Their single-crystal data also show about a three-fold rate reduction compared with polycrystals. This is presumably because of a reduction in high-angle boundary short-circuit paths achieved by highly epitaxial single-crystal scales (cf. Doychak[11]).

Compared with the body of data for undoped NiAl, the rates for the Zr-doped samples in the present study appear to be somewhat lower (up

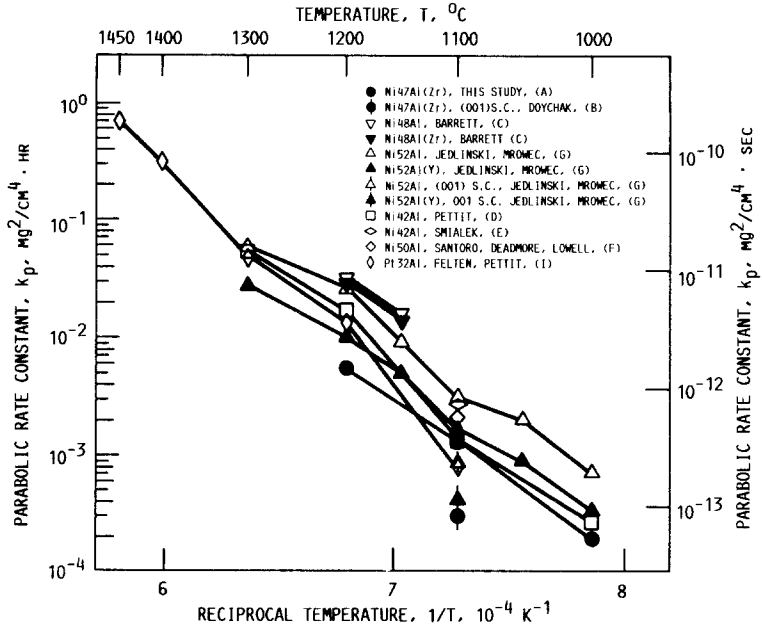

Fig. 14. Arrhenius plot of high-temperature k_p data compared with data of other NiAl studies. (See Table II for data code.)

Table II. Summary of β-NiAl Oxidation Rates

Code	Alloy	Surface	Atmosphere	Time (hr)	Temperature (°C)	k_p ($mg^2/cm^4 \cdot hr$)
A	Ni-47.2 Al (0.05 Zr)	600 grit	1 atm air	100	800	5.30×10^{-4}
	Rybicki-Smialek				900	2.27×10^{-3}
	TGA				1000	1.95×10^{-2}
					1000	1.90×10^{-4}
					1100	1.32×10^{-3}
					1200	5.53×10^{-3}
B	Ni-47.2 Al (0.05 Zr)	E.P.	1 atm air	100	800	4.0×10^{-4}
	(100) Single crystal	E.P.			1100	3.4×10^{-4}
	Doychak [11]	600 grit			1100	2.3×10^{-3}
	TGA					
C	Ni-48.3 Al	grit	1 atm air	24	1150	1.55×10^{-2}
	Ni-48.3 Al (0.1 Zr)	blasted			1200	3.11×10^{-2}
	Barrett [7]				1150	1.41×10^{-2}
	TGA				1200	2.76×10^{-2}
D	Ni-42 Al	600 grit	0.1 atm air	20	1000	2.62×10^{-4}
	Pettit [2]				1100	1.34×10^{-3}
	TGA				1200	1.68×10^{-2}
					1300	5.38×10^{-2}
E	Ni-42 Al	3 μm	1 atm air	100	1100	2.70×10^{-3}
	Smialek [5]					
	TGA, SEM					
F	Ni-50.5 Al	0.5 μm	1 atm air	100	1100	2.10×10^{-3}
	Santoro, Deadmore, Lowell [3]					
	TGA					
G	Ni-52 Al	1 μm	1 atm O_2	200	1000	7.02×10^{-4}
	Jedlinski-Mrowec				1050	1.99×10^{-3}
	(J-M) [8]				1100	3.09×10^{-3}
	SEM				1150	9.05×10^{-3}
					1200	2.67×10^{-3}
					1300	5.93×10^{-2}
	Ni-52 Al (10^{16} Y/cm^2)	1 μm	1 atm O_2	200	1000	3.29×10^{-4}
	SEM				1050	9.01×10^{-4}
					1100	1.65×10^{-3}
					1150	4.91×10^{-3}
					1200	9.96×10^{-3}
					1300	(2.72×10^{-2})
	Ni-52 Al, (001) S.C.			240	1100	9.78×10^{-4}
	Ni-52 Al, (001) S.C., (10^{16} Y/cm^2)				1100	6.02×10^{-4}
H	Ni-42 Al	1200 grit	1 atm O_2	100	900	1.66×10^{-4}
	Ni-50 Al				900	8.30×10^{-4}

Table II. Continued.

Code	Alloy	Surface	Atmos-phere	Time (hr)	Temperature (°C)	k_p (mg^2/cm^4·hr)
	Ni-55 Al Hutchings-Loretto [22] TGA				900	2.16×10^{-3}
I	Pt-32 Al (Pt_5Al_3 Phase) Felten-Pettit [19] SEM	0.05 μm	1 atm air	>100	1100 1200 1300 1400 1450	7.62×10^{-4} 1.36×10^{-2} 4.81×10^{-2} 3.08×10^{-1} 7.03×10^{-1}

to two-fold). However, the data presented by Barrett[7] for a similar NiAl+Zr alloy showed very little effect of Zr. The latter data are somewhat high and may be related to the different surface finish (grit blasted). In general, all the data are clustered in a band spanning about a factor of 3 variation. This is not unusual for slow-growing alumina scales formed on alloys produced, prepared, and oxidized by different procedures. The data for α-Al_2O_3 scales formed on the Pt_5Al_3 phase in a Pt-6 wt.% Al alloy (32 at.%) also fall within this band.[19]

Most of the k_p data presented in Fig. 14 were determined either from Δm vs $t^{1/2}$ curves or from Δm^2 vs t curves exhibiting very little transient oxidation. In the present study, oxidation at 1000 and 1100°C did show initial fast transient kinetics. Pieraggi[23] showed that, for the case of transient oxides that do not contribute to the rate control of the mature oxide, considerable error is introduced in k_p if it is determined from the slope of (weight change)^2 vs time. This is the case for transient oxides such as NiO and $NiAl_2O_4$. If the transient oxides do contribute to rate control, the above method is correct and errors would be introduced using (weight change) vs (time)$^{1/2}$. Since the initial θ-Al_2O_3 transformed entirely to the rate-controlling α-phase in the present study, we used the slope of (Δm^2-Δm_i^2) vs (t-t_i) to determine k_p.

Transition Aluminas

The existence of δ- or θ-Al_2O_3 scales is not widely reported for Ni-Al alloys. This is partly because low temperatures and short times are required to produce these phases, which otherwise transform to stable α-Al_2O_3. However, Felten and Pettit[19] reported a δ-like structure from electron diffraction of a scale formed on the Pt_5Al_3 phase of a Pt-6 wt.% Al alloy after 1200°C air oxidation for 7 min. Also, the extensive TEM work of

Doychak[10,11] in the companion study on Ni47Al+0.05Zr (at.%) single crystals has identified δ-like and θ-scales after 800°C oxidation. The formation of γ-Al_2O_3 scales has been observed more commonly. Oxidation at 500–800°C has produced γ-Al_2O_3 scales on Al,[24,25] on Al-Zn,[26] on Fe-Al,[27,31] on Ni-Al,[28] on NiCrAlZr,[19] and on CoCrAlY[30] alloys.

In the case of an Fe-12Al alloy, a discontinuity in the kinetics was observed over the 900–1050°C temperature range. This coincided exactly with a transition in scale phase from γ- to α-Al_2O_3.[31] Therefore, the same scale transition effects probably exist for both Fe-Al and β-NiAl alloys. This study has also identified θ-Al_2O_3 scales formed on Fe-25Cr-4Al at 850 and 950°C.[31]

The transition aluminas can be described as variations in the cation vacancy ordering in the defective cubic γ-Al_2O_3 pseudo-spinel structure.[32] The ordering results in a superlattice and a tripling of the unit cell dimension along the c-axis in the case of δ from γ. The cation vacancy network intrinsic to the γ, δ, and θ alumina is believed to account for rapid cation diffusion in these structures relative to α-Al_2O_3, resulting in an outward growth mechanism. The needles or whiskers observed in the present study are believed to be a vestige of outward growth due to cation lattice and surface diffusion. TEM analyses of whiskers formed on (001) NiAl+Zr single crystals have identified a $[110]_\theta$ growth direction with extremely fine 0.81- and 4.6-nm faulting parallel to the axis.[11] Voss *et al.*[33] observed Fe_2O_3 whisker formation on Fe, which also exhibited a strong crystallographic growth mechanism. These whiskers possessed an $(01\bar{1}1)$ twin habit plane, an inner longitudinal cavity, and a $[\bar{2}110]$ growth direction. Similar mechanisms may account for the $(20\bar{2})$ texture found in the transition scales of the present study.

Growth Mechanism

We might therefore expect the high θ-Al_2O_3 growth rates to have resulted from fast cation outward diffusion mechanisms. A number of studies on the transport mechanisms for alumina scales on NiAl have recently been performed. A summary of these ^{18}O radioactive tracer experiments on scale growth for β-NiAl was therefore prepared[8,34–39] (Table III). At 1000°C or less, all the ^{18}O tracer studies indicate a primary growth mechanism based on aluminum outward diffusion. It was pointed out that noble metal marker experiments, however, erroneously indicated an oxygen inward mechanism because these surface deposited markers formed islands via surface diffusion and coarsening. Upon further oxidation, the islands were simply "pushed ahead" of the oxide-gas growth interface.[35]

Although outward growth is expected for the transition aluminas at low temperature, this survey also shows primarily outward growth for

Table III. Summary of ^{18}O Tracer Studies of Alumina Growth Mechanisms[a]

Code	Alloy	Temperature (°C)	Time	Technique	Scale phase	Growth direction	Reference
A	NiAl	900	20 hr	$^{18}O(p, \alpha)^{15}N$	N.D.	Primarily Al out	Young and deWit[34]
		900	92 hr	$^{18}O(p, \alpha)^{15}N$		Primarily Al out	
		900	5 hr	Pt marker } RBS		Primarily O in[b]	
		900	N.D.	Pt marker + Al_2O_3 } RBS		Primarily Al out	
		1150	3 hr	$^{18}O(p, \alpha)^{15}N$	N.D.	Al out + O in	
				Pt marker, RBS	N.D.	O in[b]	
B	NiAl	900	32 hr	Yb, Y marker } RBS	N.D.	O in + Al out	Young *et al.*[35]
		900	32 hr	Pt. Pd, Ni marker } RBS	N.D.	O in[b]	
		1100	minutes	Pt, Pd, Ni marker } RBS	N.D.	O in[b]	
C	NiAl	1000	7 hr	$^{18}O(p, \alpha)^{15}N$	$\delta, \theta, (\alpha)$	Primarily Al out	Young and deWit[36]
	NiAl-0.07 Y	1000	7 hr	$^{18}O(p, \alpha)^{15}N$	$\delta, \theta, (\alpha)$	More Al out	
	NiAl-0.5 Y	1000	7 hr	$^{18}O(p, \alpha)^{15}N$	$\delta, \theta, (\alpha)$	Al out + O in	
D	NiAl	1000	5 min	Pd marker, AES	Amorphous	O in	Hindam and Smeltzer[37]
E	NiAl	1080	24 hr	^{18}O tracer, SIMS	N.D.	Al out + O in	Jedlinski and Mrowec[8]
	NiAl + 2×10^{14} Y/cm^2	1080	24 hr	^{18}O tracer, SIMS	N.D.	Primarily Al out	
F	NiCrAl + 0.02 Zr	1100	8 hr	$^{18}O(p, \alpha)^{15}N$	α[a]	O in (+slight Al out)	Reddy *et al.*[38]
	NiCrAl + 0.07 Zr	1100	8 hr	$^{18}O(p, \alpha)^{15}N$	α	O in	
	NiCrAl + 0.27 Y	1100	8 hr	$^{18}O(p, \alpha)^{15}N$	α	O in	
G	FeCrAl	1080	28 hr	$^{18}O(p, \alpha)^{15}N$	N.D.	Primarily Al out	Huntz[39]
	FeCrAlY	1080	28 hr	$^{18}O(p, \alpha)^{15}N$	N.D.	Primarily Al out, +some O in	

[a] From Khan *et al.*[40]
[b] Noble metal marker experiments disagree with ^{18}O tracer results.

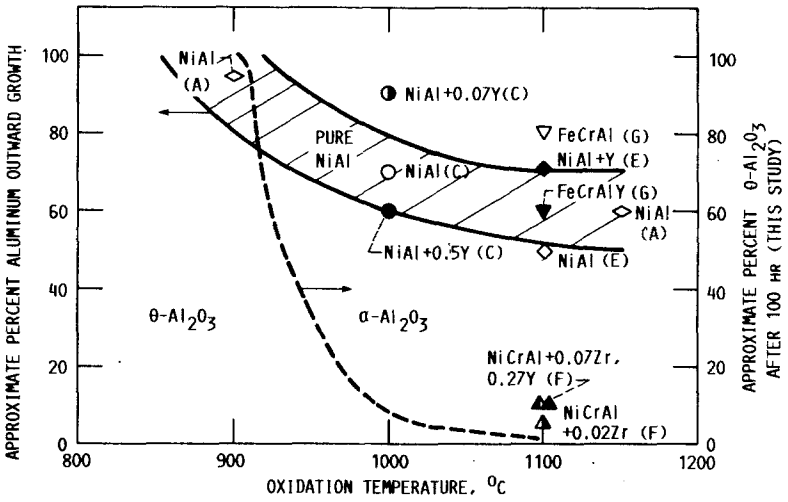

Fig. 15. Temperature and composition effects on Al_2O_3 growth mechanisms provided by ^{18}O tracer studies. (See Table III for data code.)

β-NiAl at 1080–1150°C as well (Fig. 15). The hatched band represents a semiquantitative estimate of the relative amounts of aluminum outward and oxygen inward growth. These estimates were taken from ^{18}O and ^{16}O depth profiles or from α-particle count rate versus energy profiles produced by the $^{18}O(p, \alpha)^{15}N$ proton activation technique. The picture is further complicated by both increases and decreases in the oxygen inward contribution caused by increasing yttrium additions.[36]

Also shown on this curve are the relative θ–α contents obtained from the XRD data of the present study. Note that Young and de Wit[36] (C) did identify primarily δ or θ scales after the 7 hr oxidation at 1000°C. The extent of transition aluminas present in the other ^{18}O studies is not known. The high component of outward growth for high temperature α-scales is in strong contrast to the inward growing scales found for NiCrAlY, Zr alloys.[39] The inward growth is commonly accepted as a short-circuit grain-boundary mechanism resulting from fine grain scales. Outward growth has been proposed for NiAl and Pt_2Al oxidation because of the large-grain single-crystal areas.[9,19] Indeed, microstructure and scale phase content may account for many of the apparent discrepancies in Fig. 15.

Microstructure and the Transformation to α-Al_2O_3

The distinctive scale microstructure for β-NiAl oxidation is the network of oxide ridges resulting in a cellular, weblike, or cross-hatched appearance. The evolution of this structure has recently been described in detail by

Doychak on the basis of TEM, STEM, and SEM observations. Nucleation and radial growth of α-Al_2O_3 cells occurs at the surface of the transition alumina scales. This transformation is accompanied by a large volume contraction, resulting in cracking, porosity, and dislocations.

An idealized schematic of a fully transformed α-cell is shown in Fig. 16 taken from the work of Doychak.[11] At the base of the transformation cracks, a fine-grained polycrystalline oxide forms as a substantial growth ridge into the alloy. The thin central region of the cell is a mosaic of low-angle boundary subgrains and can be thought of as a deformed single crystal containing dislocation networks. Some subgrains have greater misorientations and result in short-circuit aluminum diffusion and spoke like ridges at the gas surface. Relatively large-angle boundaries (10°) are observed at the edges of cells, the last regions to transform and impinge on neighboring cells. These boundaries show a substantial degree of impurities plus both inward and outward growth, as evidenced by the ridges on both surfaces of the scale.

Surface smoothing of the θ-Al_2O_3 nodules or needles occurs simultaneously with the transformation. This process has been analyzed by Doychak as a spheroidization phenomenon driven by a reduction in surface energies.[11]

The morphology of Fig. 16 is very inhomogeneous and clearly may be responsible for a number of growth mechanisms occurring in concert, e.g., short-circuit outward growth primarily at grain boundaries, lattice outward growth within cells, and inward short-circuit growth beneath cracks and

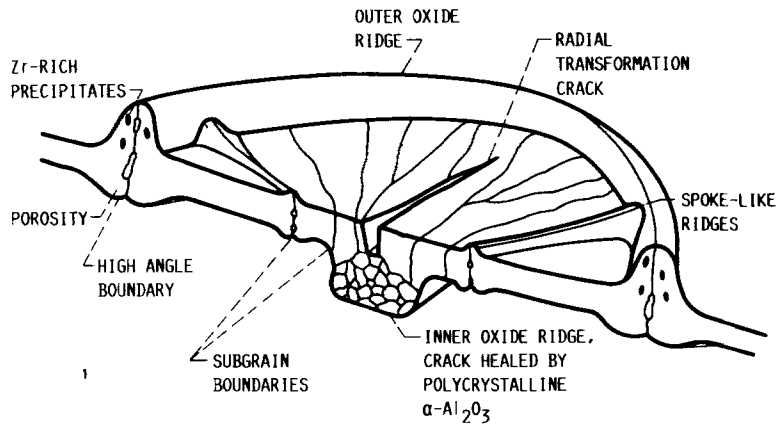

Fig. 16. Schematic section of a fully transformed cell of α-Al_2O_3 showing ridge development and cracking. (From Doychak.[11])

cell boundaries. These complexities may allow for the large mix of growth mechanisms reported in the tracer studies at high temperatures (Fig. 15). By contrast, the uniformly fine-grain scales reported for NiCrAl+Y,Zr alloys resulted in primarily inward-growing scales.[38]

Thus, for the complex case of Al_2O_3 scales on NiAl, the description of growth mechanisms by ^{18}O tracer studies needs to be coupled with X-ray diffraction (XRD) and SEM characterization of the scales and vice versa. This will enable the transport mechanisms to be distinguished for θ- and α-scales as well as between scales with or without highly developed ridge structures, seen to vary widely with metal grain orientation.[9,11] The preponderance of aluminum outward growth demonstrated by Table III is believed to result from the presence of cubic transition alumina at low temperatures and short times and from short-circuit cation diffusion accompanying ridge formation.

It should also be pointed out that the ridge structure, while quite distinctive in appearance at short times, does not grow outward in proportion to the rest of the scale thickness, see, e.g., the cross sections of Hindam and Smeltzer.[9] Thus, the substantial aluminum outward growth shown for NiAl oxidized at the higher temperatures, 1080°C for 24 hr and 1150°C for 3 hr (Table III), may diminish at longer times for more mature scales.

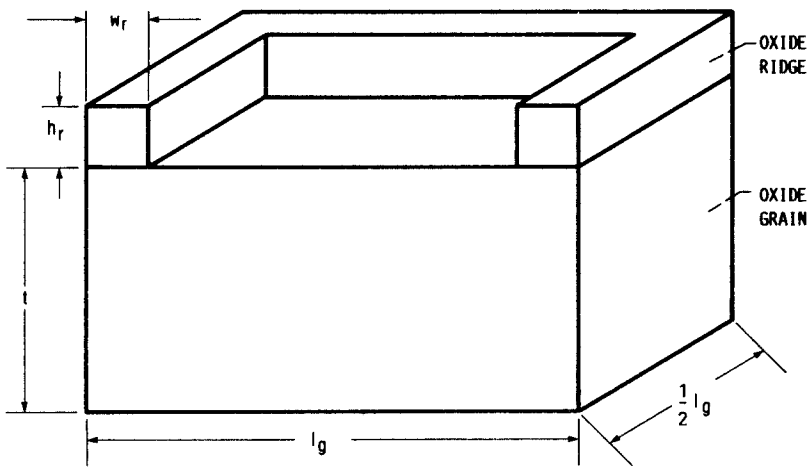

$$\text{RIDGE VOLUME} = h_r \times w_r \times 2\, l_g$$

$$\text{GRAIN VOLUME} = t \times 1/2\, l_g^{\,2}$$

$$\% \text{ RIDGE} = \frac{4\,(hw)_r}{t l_g + 4\,(hw)_r} \times 100\%$$

Fig. 17. Idealized section of a half-grain showing relative ridge volume.

This factor and the effect of oxide grain size on the importance of the ridge network to overall scale growth is shown schematically in Figs. 17 and 18. In Fig. 17, a half-section of a square grain ($\frac{1}{2}l_g \times l_g$) and a square "doughnut" (h_r by w_r) of grain-boundary ridge is drawn for a scale of thickness (t). The relative volume of ridge to the total scale is thus:

$$\text{Percentage ridge volume} = \frac{4h_r w_r}{(tl_g + 4h_r w_r)} \times 100\%$$

The following analysis approximates the ridge cross section to be constant at 1×1 μm, which is close to the experimental observations in this study. Thin coatings can have a substantial ridge contribution to overall growth, especially for fine-grain scales ($l_g < 5$ μm) (Fig. 18a). Coarse-grain and thick scales ($t = l_g = 10$ μm) (Fig. 18d) have a minimal contribution because of the ridges, even though they appear as a quite distinctive feature. As the ridge spacing decreases for finer grains, the surface will appear to have a dimpled or porous texture, as suggested by F. S. Pettit (private

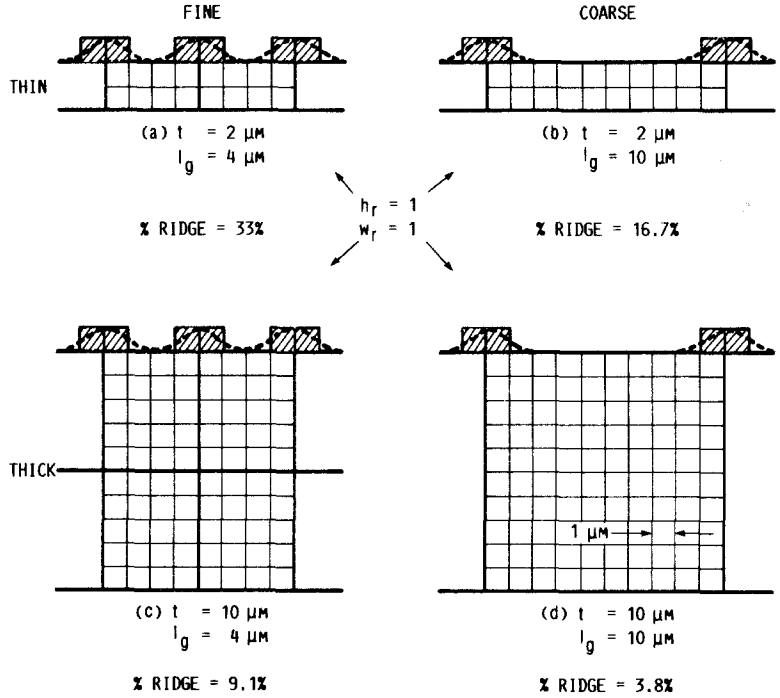

Fig. 18. Relative ridge volumes for thin (a,b), thick (c,d), fine-grain (a,c), and coarse-grain (b,d) scales. A fixed ridge width and thickness has been assumed for the sake of illustration.

communication, 1979) and often observed.[5,19,37,41,42] The finest grain sizes will cause the ridges to impinge on each other, making them indistinguishable as a surface feature.

Ridged Scales

The above picture of ridge formation is basically in agreement with the model previously proposed by Hindam and Smeltzer.[9] These investigators suggested that the thin α-platelets resulted from recrystallization of an initial microcrystalline film to form an epitaxial scale. As nuclei grew and impinged, the boundary regions of "disarrayed oxide induced by faulting" became ridges dominated by cation and anion short-circuit diffusion. Our present work and the studies by Doychak have shown that the initial films were oriented transition aluminas; otherwise, the models are similar.

These views differ substantially from those put forward by Homma *et al.*,[43] who suggested an effect of the NiAl substructure on the generation of the ridge network. X-ray topographic observations of parallel arrays of dislocations with spacings on the order of the oxide ridge spacings were the evidence for this proposal. However, the rectangular geometry of the dislocation arrays and the weblike mosaic structure of the ridges do not appear to be well correlated.

Mrowec *et al.*[17] showed ridged structures on NiAl oxidized at 1100 and 1200°C. Here lateral growth of the ridges occurred, eventually consuming the flat thin regions between ridges. The end result was a roughened or dimpled texture (Fig. 18a,c). However, dimples also occurred within the ridge oxide as well. They showed that ion implantation of Y and La retarded this lateral overgrowth and eventually prevented the ridge structure at a dose of 2×10^{16} ions/cm^2. These effects were explained as an elimination of oxygen inward grain-boundary diffusion and lateral growth within the scale[8,17] (see Table III).

The earliest report of the ridged α-Al_2O_3 scales was for the Pt_2Al phase of a Pt-6Al alloy.[19] Oddly enough, the Pt_5Al_3 phase in this alloy, which did form an oriented δ-like scale similar to those in the present work and in Doychak's studies, transformed to a fine-grained α-scale having no ridge structure. The critical factor determining whether a ridge network is developed may simply be whether the stable α-nuclei are sparse enough, e.g., separated by 10 μm or greater, to permit distinct delineation. What promotes sparse nucleation in the case of scales on NiAl or Pt_2Al is not known. For the case of NiCrAl+Y,Zr oxidation at 1100°C, it has been shown that $Ni(Al,Cr)_2O_4$ transients form and discontinuous nucleation of α-Al_2O_3 occurs *beneath* these transients.[29] Thus, a free surface may have

been unavailable for the nucleation of α, which has been shown to be a preferred site in transition alumina scales or in bulk oxides.[15,21]

Some very interesting observations regarding ridge structure have also been made for FeCrAl+Zr (Hoskins 875) by Basu.[18] They can be summarized as follows:

1. A cellular network formed at 1100°C, which decreased in cell size with oxidation time. This occurred because both the cell frequency and ridge thickness increased. At 40 hr, no remnant of cells or dimples was evident; total impingement had occurred. (An example of a partially obscured cell structure is shown in Fig. 19.)
2. Preannealing in vacuum encourages the weblike ridge structure to form after 10 hr at 1100 or 1200°C, exactly like those reported in this study.

Widely differing Al_2O_3 ridge morphologies can thus be possible, especially for the shorter oxidation times. It is believed that the ridge or cellular structure observed on FeCrAl for $t < 40$ hr may be the reason

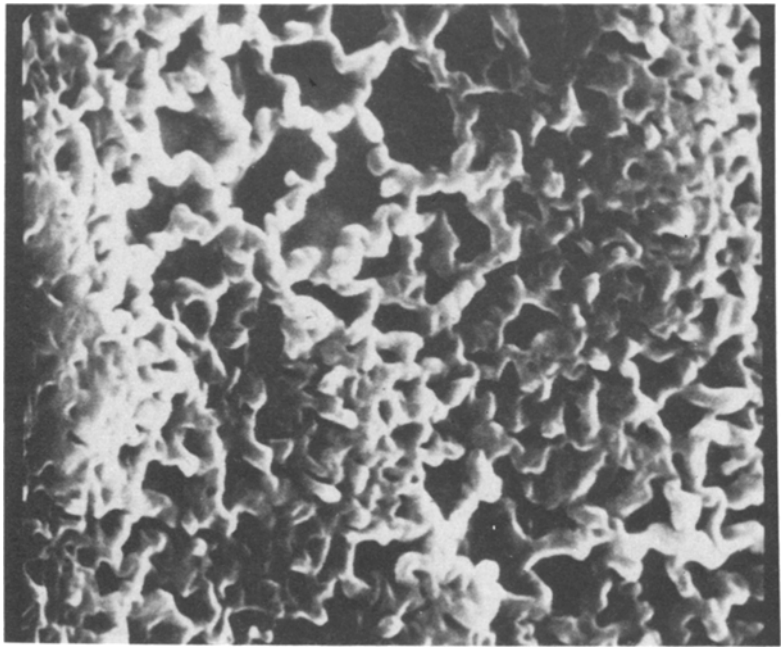

Fig. 19. Cellular ridge structure and oxide dimples formed on FeCrAl+Zr after 10 hr at 1100°C.

outward aluminum diffusion was observed in ^{18}O tracer studies by Basu[18] (1100°C, 36 hr) and Huntz[39] (1080°C, 28 hr) (Table III).

Ridged Scales in Other Systems

Morphologies similar to those of Al_2O_3 scales have been observed in NiO scales grown on Ni.[44] Here a network of fast growing fine-grain regions accounted for the ridges in contrast to areas having a large grain scale. Also, both cellular and dimpled scales have been observed for Fe_2O_3 formed on Fe and for Fe_3O_4 scales formed on steel.[45,46]

A dramatic ridge network develops during the sulfidation of manganese, even though a phase transformation in the scale is not apparent.[47] At 600–900°C, a very distinct sulfide ridge network was formed at the boundaries of large 30-μm grains. Below 500°C, the scales were very fine grained (1–2 μm) and exhibited dimpled or porous scales similar to the Al_2O_3 scale formed on undoped NiCrAl at 1100°C.[38] The Arrhenius plot for MnS growth rate showed a low-temperature branch, indicating growth primarily by grain-boundary diffusion, as well as a high-temperature branch (>700°C) dominated by lattice diffusion because of the very large grains formed here. The ridge network was distinctive in appearance up to 1100°C, even though boundary diffusion was not believed to be a significant contribution above 700°C. Thus, the discussion of grain size, thickness, and transport factors (Fig. 18) appears to apply to this case.

It is expected that the diversity of systems producing diverse dimpled, cellular, or weblike ridged scale morphologies may ultimately preclude a generalized mechanism. Thus, the model proposed in Fig. 16 may be appropriate for NiAl+Zr but would require modifications to accurately describe other scales and alloys.

CONCLUSIONS

Isothermal oxidation of β-NiAl+Zr has been performed over the temperature range 800–1200°C and studied by TGA, XRD, and SEM. An Arrhenius plot of the growth kinetics, k_p vs $1/T$, exhibited a discontinuous decrease of two orders of magnitude with increase in temperature at 1000°C. Two separate lines were used to describe the kinetics both above and below this temperature. The same decrease occurred with oxidation time at 1000°C. Both events were concurrent with a change in scale phase content from θ to α-Al_2O_3. We conclude that the oxidation of β-NiAl is accompanied by a phase transformation in the scale that is most noticeable in the vicinity of 1000°C. This appears on an Arrhenius plot as a transition in kinetics from control by θ to control by α-Al_2O_3.

The phase transformation was also concurrent with dramatic changes in scale morphology, i.e., a whisker topography changed into flat plates with radial cracks and eventually into a network of ridges. We conclude that the cracks are caused by transformation stresses and that the ridges are boundaries between adjacent plates, as suggested by Doychak. It is believed that the ridges are also evidence for short-circuit outward diffusion of aluminum, which has been documented in a number of recent ^{18}O tracer studies on NiAl. Thus, the peculiar structure of scales formed on NiAl may account for the differences in growth mechanisms for scales formed on NiAl and those formed on MCrAlY alloys.

This study, coupled with previous reports in the literature, suggests that fast-growing, metastable, transition alumina scales commonly occur during oxidation of Ni–Al, Fe–Al, and MCrAl alloys at temperatures below 1100°C. Observations made at these temperatures cannot be directly attributed to the stable α-Al_2O_3 scales formed at higher temperatures.

ACKNOWLEDGMENTS

The authors appreciate many helpful discussions of scale morphology with J. Doychak.

REFERENCES

1. I. Baker and P. R. Munroe, *J. Met.* **40**, 28 (1988).
2. F. S. Pettit, *Trans. TMS-AIME* **239**, 1296 (1967).
3. G. J. Santoro, D. L. Deadmore and C. E. Lowell, NASA TN D-6414 (1971).
4. C. E. Lowell and G. J. Santoro, NASA TN D-6838 (1972).
5. J. L. Smialek, *Metall. Trans. A* **9**, 309 (1978).
6. C. S. Barrett and C. E. Lowell, U.S. Patent **4**, 610, 736 (1986).
7. C. S. Barrett, *Oxid. Met.* **30**, 361 (1989).
8. J. Jedlinski and S. Mrowec, *Mater. Sci. Eng.* **87**, 281 (1987).
9. H. M. Hindam and W. W. Smeltzer, *J. Electrochem. Soc.* **127**, 1622 (1980).
10. J. K. Doychak, Masters thesis, Case Western Reserve University, Cleveland, Ohio (1984); also NASA CR-174756.
11. J. K. Doychak, Doctoral thesis, Case Western Reserve University, Cleveland, Ohio (1986); also NASA CR-175097.
12. J. K. Doychak, in *Proceedings of the Forty-second Electron Microscopy Society of America Meeting*, G. W. Bailey, ed. (San Francisco Press, San Francisco, 1984), p. 598.
13. J. K. Doychak, J. L. Smialek, and T. E. Mitchell, in *International Congress on Metallic Corrosion*, Vol. 1 (National Research Council of Canada, Ottawa, Canada, 1984, p. 35.
14. J. K. Doychak, T. E. Mitchell, and J. L. Smialek, in *High-Temperature Ordered Intermetallic Alloys*, MRS Symp. Proc. Vol. 39, C. C. Kock, C. T. Liu, and N. S. Stoloff, eds. (Materials Research Society, Pittsburgh, 1985), p. 475.
15. J. K. Doychak, J. L. Smialek, and T. E. Mitchell, *Metall. Trans. A* (1989, in press).
16. J. Jedlinski, in *Proceedings of the Tenth International Congress on Metallic Corrosion*, Madras, India, K. I. Vasu and K. Balikrishnan, eds. Karaikudi, India (1987), p. 3709.
17. S. Mrowec, A. Gil, and A. Jedlinski, *Werkst. Korros.* **38**, 563 (1987).
18. S. N. Basu, Masters thesis, Case Western Reserve University, Cleveland, Ohio (1984); also NASA CR-174796.

19. E. J. Felten and F. S. Pettit, *Oxid. Met.* **10**, 189 (1976).
20. A. Ruiz, Doctoral thesis, Case Western Reserve University, Cleveland, Ohio (1986).
21. W. T. Donlon, T. E. Mitchell, and A. H. Heuer, *J. Mater. Sci.* **17**, 1389 (1982).
22. R. Hutchings and M. H. Loretto, *Met. Sci.* **12**, 503 (1978).
23. B. Pieraggi, *Oxid. Met.* **27**, 177 (1987).
24. R. T. Phelps, E. A. Gulbransen, and J. W. Hickman, *Indust. Eng. Chem. Anal. Ed.* **18**, 391 (1946).
25. J. I. Eldridge, R. J. Hussey, D. F. Mitchell, and M. J. Graham, in *Fundamental Aspects of High Temperature Corrosion*, Vol. II Electrochem. Soc. Proc. 86-9, Z. A. Munir and D. Cubicciotti, eds. (Electrochemical Society, Pennington, New Jersey, 1986), p. 226.
26. G. M. Scamans and E. P. Butler, *Metall. Trans. A* **6**, 2055 (1975).
27. W. E. Boggs, *Oxid. Met.* **10**, 277 (1976).
28. M. Sakiyama, P. Tomaszewicz, and G. R. Wallwork, *Oxid. Met.* **13**, 311 (1979).
29. J. L. Smialek and R. Gibala, *Metall. Trans. A* **14**, 2143 (1983).
30. J. A. Sprague, V. Provenzano, and A. A. Smidt, *Thin Solid Films* **95**, 57 (1982).
31. W. C. Hagel, *Corrosion* **21**, 316 (1965).
32. A. Dauger and D. Fargeot, *Radiat. Effects* **74**, 279 (1983).
33. D. A. Voss, E. P. Butler, and T. E. Mitchell, *Metall. Trans. A* **13**, 929 (1982).
34. E. W. A. Young and J. H. W. de Wit, *Solid State Ionics* **16**, 39 (1985).
35. E. W. A. Young, J. P. M. van Vliet, and J. H. W. de Wit, in *Reactivity of Solids*. Parts A and B, P. Barret and L. C. Dufour, eds. (Elsevier, New York, 1985), p. 229.
36. E. W. A. Young and J. H. W. de Wit, *Oxid. Met.* **26**, 351 (1986).
37. H. M. Hindam and W. W. Smeltzer, *Oxid Met.* **14**, 337 (1980).
38. K. P. R. Reddy, J. L. Smialek, and A. R. Cooper, *Oxid. Met.* **17**, 429 (1982).
39. A. M. Huntz, *Mater. Sci. Eng.* **87**, 251 (1987).
40. A. S. Khan, C. E. Lowell, and C. A. Barrett, *J. Electrochem. Soc.* **127**, 670 (1980).
41. J. L. Smialek and R. Gibala, in *High Temperature Corrosion*, NACE-6, R. A. Rapp, ed. (National Association of Corrosion Engineers, Houston, Texas, 1983), p. 274.
42. J. K. Tien and F. S. Pettit, *Metall. Trans.* **3**, 1587 (1972).
43. T. Homma, H. M. Hindam, Y. Pyun, and W. W. Smeltzer, *Oxid. Met.* **17**, 223 (1982).
44. J. C. Pivin, J. Morvan, and D. Mairey, *Acta Metall.* **32**, 2203 (1984).
45. D. Caplan, R. J. Hussey, G. I. Sproule, and M. J. Graham, *Corros. Sci.* **21**, 689 (1981).
46. N. J. Cory and T. M. Herrington, *Oxid. Met.* **28**, 237 (1987).
47. M. Danielewski, *Oxid. Met.* **25**, 51 (1986).